Research Square

Preprints are preliminary reports that have not undergone peer review.
They should not be considered conclusive, used to inform clinical practice,
or referenced by the media as validated information.

Tabletop EUV reflection dual-polarisation ptychography enables high-throughput nanoscale material-mapping and angstrom-scale profilometry

Daniel Penagos Molina

santiago.penagos@uni-jena.de

Institute of Applied Physics - Friedrich-Schiller-University Jena https://orcid.org/0000-0003-4329-2421

Mahmoud Abdelaal

Institute of Applied Physics - Friedrich-Schiller-University Jena

Wilhelm Eschen

CU Boulder, JILA

Chang Liu

Institute of Applied Physics - Friedrich-Schiller-University Jena

Leona Licht

Institute of Applied Physics - Friedrich-Schiller-University Jena

Themistoklis Sidiropoulos

Helmholtz Institute Jena

Robert Klas

Fraunhofer Institute for Applied Optics and Precision Engineering

Lars Loetgering

ZEISS Research Microscopy Solutions

Richard Busch

Fraunhofer Institute for Microstructure of Materials and Systems

Thomas Höche

Fraunhofer Institute for Microstructure of Materials and Systems

Jens Limpert

Institute of Applied Physics and Abbe Center of Photonics, Friedrich-Schiller-University Jena

Jan Rothhardt

Institute of Applied Physics and Abbe Center of Photonics, Friedrich-Schiller-University Jena

---

Article

Keywords: ptychography, tabletop, polarisation, material-mapping

Posted Date: May 8th, 2026

DOI: https://doi.org/10.21203/rs.3.rs-9267824/v1

License: This work is licensed under a Creative Commons Attribution 4.0 International License.
Read Full License

Additional Declarations: There is **NO** Competing Interest.

Tabletop EUV reflection dual-polarisation ptychography enables high-throughput nanoscale material-mapping and angstrom-scale profilometry

Daniel S. Penagos Molina[1,2,3*†], Mahmoud Abdelaal[1†], Wilhelm Eschen[1,2,3], Chang Liu[1,2,3], Leona Licht[1,2,3], Themistoklis P.H. Sidiropoulos[1,2,3], Robert Klas[1,2,3,4], Lars Loetgering[5], Richard Busch[6], Thomas Höche[6], Jens Limpert[1,2,3,4], Jan Rothhardt[1,2,3,4]

[1]Institute of Applied Physics and Abbe Center of Photonics, Friedrich-Schiller-University Jena, Albert-Einstein-Straße 15, Jena, 07745, Germany.
[2]Helmholtz-Institute Jena, Fröbelstieg 3, Jena, 07743, Germany.
[3]GSI Helmholtzzentrum für Schwerionenforschung, Planckstraße 1, Darmstadt, 64291, Germany.
[4]Fraunhofer Institute for Applied Optics and Precision Engineering, Albert-Einstein-Straße 7, Jena, 07745, Germany.
[5]ZEISS Research Microscopy Solutions, Carl Zeiss Promenade 10, Jena, 07745, Germany.
[6]Fraunhofer Institute for Microstructure of Materials and Systems, Walter-Hülse-Straße 1, Halle, 06120, Germany.

*Corresponding author(s). E-mail(s): santiago.penagos@uni-jena.de;
†These authors contributed equally to this work.

Abstract

Extreme-ultraviolet (EUV) reflection ptychography can deliver nanoscale surface metrology with material-specific contrast, but its practical use has been limited by slow acquisition and the need for multi-angle datasets for reliable material identification. Here, we demonstrate Brewster-range, polarisation-resolved EUV reflection ptychography: a single polarisation achieves sub-100 nm diffraction-limited resolution and Å-scale height precision over $\sim$ **90** µ**m** $\times$ **90** µ**m** fields of view, while the two-polarisation response at a single incidence angle, enables

material identification through enhanced diattenuation and retardance. Driven by a milliwatt-class tabletop high-harmonic-generation (HHG) source and structured illumination, we reach throughputs up to $\sim$ **100 Mpx h^{-1}**, about two orders of magnitude higher than previous tabletop EUV reflection ptychography and comparable to synchrotron-based implementations. This places EUV reflection ptychography in a synchrotron-like throughput regime on a laboratory platform, making it a practical tool for routine, non-destructive nanoscale material characterisation in systems ranging from two-dimensional materials and metasurfaces to magnetic multilayers and catalytic surfaces, and for future ultrafast pump–probe studies.

Keywords: ptychography, tabletop, polarisation, material-mapping

1 Introduction

Nanoscale characterisation of surfaces with element- and chemical contrast is central to many areas of research and technology. These include semiconductor manufacturing and EUV lithography, as well as studies of two-dimensional quantum materials, complex oxide heterostructures, magnetic multilayers and domain structures, nanophotonic metasurfaces, and catalytic or energy-related surfaces [1–9]. In semiconductor manufacturing and EUV lithography, sub-20 nm lateral resolution at the operational wavelength is required to detect patterning- and metal pitch defects [10, 11]. Studies of two-dimensional materials and complex oxides demand Å-scale height sensitivity [4] and element-specific contrast to resolve subtle changes in stacking, composition, and interfacial structure, while magnetic multilayers, metasurfaces, and catalytic or energy-related surfaces benefit from methods that can distinguish near-surface material states and buried interfaces [7–9].

To meet these needs, existing surface and near-surface characterisation techniques span non-contact optical profilometry (e.g. white-light interferometry) for fast, large-area topography [12, 13], scanning-probe methods (e.g. atomic force microscopy) for Å-scale height precision [14], electron-beam microscopy for high-resolution imaging with X-ray microanalysis (e.g. SEM/EDX) [15], electron spectroscopies for nanometre-scale depth and chemical-state sensitivity (e.g. XPS) [16], and ion- or mass-spectrometry methods for ultra-surface-sensitive chemical mapping and depth profiling (e.g. ToF-SIMS) [17]. Each technique excels in a particular niche, but they inevitably involve trade-offs between field of view, throughput, and invasiveness.

To summarise, there is a steady demand for new analysis techniques with nanoscale lateral resolution, material sensitivity, and throughput. A method with these capabilities, compatible with opaque substrates, and enabling non-destructive operation on a tabletop platform, would provide a valuable complement to existing tools across the research areas outlined above, where access to both spatial structure and local optical response is crucial, while reducing sample transfers between instruments.

Coherent diffractive imaging, and in particular ptychography [18], offers a route to address this gap. It is a lensless computational imaging method in which an object is

scanned with confined coherent illumination in overlapping regions [19]. A pixelated detector records the diffracted intensities in either transmission or reflection geometries, and an iterative algorithm reconstructs a complex-valued representation of the object from the intensity-only diffraction patterns. Because it does not rely on imaging lenses, it bypasses the need for costly short-wavelength optics, and the achievable spatial resolution is set by the numerical aperture (NA) and the employed wavelength. When combined with extreme-ultraviolet (EUV) wavelengths (10–100 nm), reflection ptychography can provide sub-100-nm lateral resolution together with quantitative phase information [20–25]. The reconstructed object is a complex-valued field at the sample surface that encodes both the local amplitude and phase of the reflected wave. At EUV photon energies, the refractive indices of many materials vary strongly near absorption edges, and the penetration depth in solids is typically only a few to a few tens of nanometres. As a result, small changes in roughness, surface height, composition, or thickness lead to large variations in the reflected amplitude and phase. For a given sample, this can yield significantly stronger contrast in the EUV spectral range than at visible or hard X-ray energies, making EUV reflection ptychography especially relevant for quantitative, surface-sensitive metrology, buried defects inspection [26], and in pump–probe schemes, for probing ultrafast dynamics in the near-surface region [27].

Today, tabletop EUV sources based on high-harmonic generation (HHG) can be integrated directly into laboratory environments, enabling nanoscale EUV measurements with high cadence and close co-location with nanofabrication tools [19]. Previous work with compact EUV sources has demonstrated reflection ptychography for nanoscale surface metrology [20–25] and, more recently, for material characterisation using multiple angles of incidence and polarisations in ptycho-ellipsometry schemes [28]. These studies have shown that EUV reflection ptychography can, in principle, retrieve optical constants and layered structures, but they also face a strong bottleneck in throughput. In practice, three factors dominate: the intrinsically low reflectivity of most materials at EUV wavelengths [29], the modest photon flux of typical tabletop HHG sources compared with synchrotrons or free-electron lasers [30, 31], and the need to acquire multi-angle datasets. Together, these limitations lead to acquisition times of hours for fields of view on the order of 0.1 mm^2.

In this work, we use a high-flux, milliwatt-class tabletop HHG source at 26.7 eV [32] and exploit the strong material contrast available in the Brewster range near an angle of incidence (AOI) of 45° (see Fig. 1). This combination allows us to realise a conceptually simple EUV reflection ptychography scheme that requires only two polarisation measurements at a single angle of incidence for reliable material identification, while achieving diffraction-limited lateral resolution and imaging throughputs of up to $\sim 100\ \mathrm{Mpx\,h^{-1}}$. This corresponds to acquisition rates of about two orders of magnitude higher than those of previous tabletop EUV reflection ptychography[20–25], and is comparable to reported synchrotron experiments [33–36]. Importantly, the two-polarisation scheme at a fixed angle of incidence eliminates the need to rotate the sample and to track the specular beam with a rotating detector, thereby relaxing mechanical constraints and sample alignment. The increased photon flux also enables the use of a structured illumination probe in a reflection geometry, implemented

with an amplitude mask, while keeping acquisition times practical. This structured probe improves the conditioning of the ptychographic reconstruction and enhances its robustness [37–41]. This combination of experimental and algorithmic advances pushes tabletop EUV reflection ptychography into a synchrotron-like throughput regime on a laboratory platform, making nanoscale material characterisation feasible as a routine, co-located tool rather than only during limited beamtime at large-scale facilities.

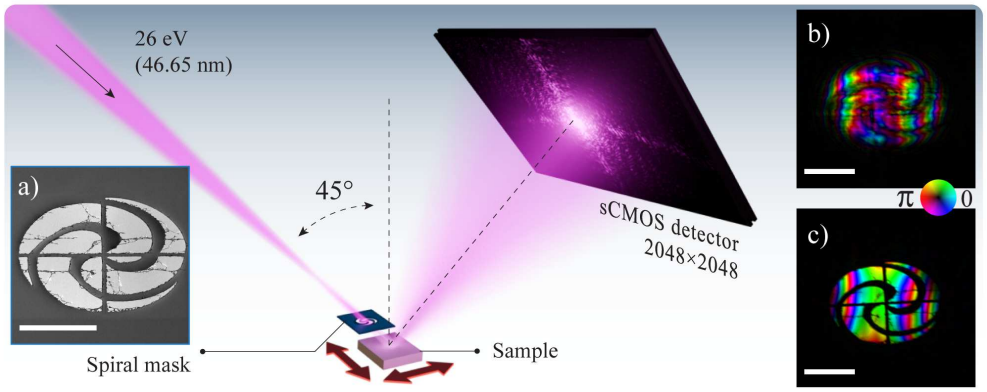


Fig. 1 Experimental geometry for EUV reflection ptychography. An EUV beam incident at AOI 45° is modulated by a spiral amplitude mask 370 µm upstream of the sample. The specimen is scanned in overlapping positions and the reflected signal is recorded in a non-coplanar geometry by a pixelated detector. Insets: (a) SEM micrograph of the spiral mask, (b) reconstructed complex probe; hue encodes phase, brightness encodes amplitude, and (c) back-propagated wavefront at the mask plane. Scalebar is 30 µm.

2 Results

We first validate our Brewster-range EUV reflection ptychography scheme as a quantitative surface metrology tool. We then demonstrate single-angle, two-polarisation material identification, and finally assess the performance of our results in terms of the imaging throughput.

2.1 EUV surface metrology

Our diffraction geometry is shown in Fig. 1, and a more detailed description of the experimental setup is given in the Methods. In short, an EUV beam at 46.7 nm (26.7 eV) is incident on the sample at an angle of 45°. Its wavefront is modulated by a spiral amplitude mask placed 370 µm upstream of the surface, producing a structured illumination probe on the sample [39]. The diffracted intensity is recorded on a pixelated sCMOS detector positioned at a distance of $\sim$ 43 mm from the sample. Insets (a), (b), and (c) in Fig. 1 show a SEM micrograph of the fabricated spiral mask, the reconstructed complex-valued illumination probe, and the back-propagated wavefront at the mask plane, respectively.

For surface metrology, we first measured a standard USAF resolution test target consisting of chromium features on a fused-silica substrate. The reconstructed phase from EUV reflection ptychography is converted into a height profile via the optical path difference (OPD) formalism [21] (see Supplemental document). We compare this height map with standard surface metrology techniques and summarise the results in Fig. 2.

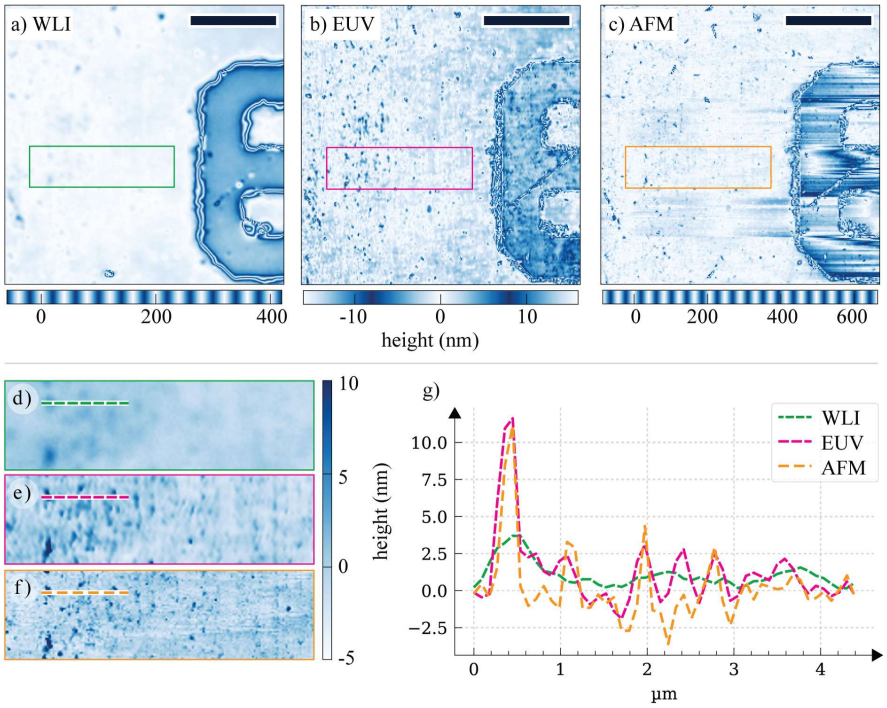


Fig. 2 Comparison of EUV surface metrology with standard techniques. First row: WLI topography (100× objective) (a), height map from EUV reflection ptychography (b), obtained by converting the reflection-geometry optical path difference (OPD) into height, and AFM topography (c). Scale bar: 10 µm. Second row: (d-f) zoomed-in insets from each technique, used to qualitatively assess the spatial resolution. (g) Line profiles along the marked regions, comparing the height traces from WLI, EUV ptychography, and AFM.

The top row of Fig. 2 shows the same field of view (FOV) measured with white-light interferometry (WLI, 100× objective, panel a), EUV ptychography (height map derived from the reconstructed phase, panel b), and atomic force microscopy (AFM, panel c). Because the ptychographic phase is defined modulo 2π, extending the dynamic range of the EUV height map requires phase-unwrapping algorithms (see Supplemental document). In the lower panels of Fig. 2d-f), we highlight a region of interest to qualitatively assess the spatial resolution. In this region, the EUV ptychography reconstruction resolves fine surface features that are blurred in the WLI data and does not exhibit the scan-line artefacts visible in the AFM image [42] (panel g).

We note that such AFM scan-line artefacts can, in principle, be mitigated with specialised post-processing, but this typically requires additional analysis steps and may distort extended surface features. The line profiles in Fig. 2g) show good agreement between the EUV ptychography and AFM height traces, particularly in the positions and relative amplitudes of the main peaks and valleys. Small discrepancies may arise because the phase-to-height conversion strictly assumes a single, homogeneous material, whereas the USAF target may exhibit local variations in composition or mass density, which would alter the local phase response. By contrast, the WLI trace captures only the broader topography and smooths out the finer features. The spatial resolution of this measurement is $\sim$ 90 nm, estimated via Fourier ring correlations (FRC) and half-bit-criteria [43]. In addition, using two independent measurements, we estimated the phase restoration uncertainty to be $\sigma_\phi \sim 74$ mrad over a 90 µm $\times$ 90 µm field of view and $\sim$ 36 mrad for an area of 9 µm $\times$ 9 µm (see Supplemental document). This phase uncertainty translates, respectively, into axial height uncertainties of $\sim$ 4 Å and $\sim$ 2 Å using the OPD relation (see Supplemental document). This corresponds to height changes that are about 10^5 times smaller than the scanned area and more than two orders of magnitude smaller than the reconstruction pixel size.

To summarise, these measurements establish that for a nominally monolithic surface, EUV reflection ptychography can recover topography with accuracy comparable to AFM while offering a field of view that is, in practice, limited only by the scan extent rather than by the intrinsic resolution–FOV trade-offs of WLI and AFM. This validates the use of phase-derived height maps as a quantitative surface metrology tool.

2.2 Material identification using p/s-polarisation contrast

We now turn to surface material identification using polarisation-resolved reflection ptychography. For this purpose, we seek a sample in which the substrate and nominal topography are well defined, but whose surface also carries thin, nanoscale contaminants. Such mixture represent a stringent test for EUV-based material discrimination: they are confined to the near-surface region, can be chemically distinct from the substrate, and are often difficult to detect with more deeply penetrating or laterally averaging probes such as SEM–EDX [15], hard X-ray reflectometry [44], or even TEM-based spectroscopies without destructive cross-sectioning.

We use a test structure consisting of a binary topographic "Abbe portrait" patterned on a Si_3N_4 membrane using conventional FIB milling (see Methods). A scanning electron micrograph of the Abbe portrait is shown in Fig. 3a). In this case, the substrate is known, and the topography is nominally binary, while the SEM/FIB processing is expected to introduce thin near-surface contaminants. This combination of a well-defined substrate with realistic yet constrained near-surface modifications makes the Abbe portrait a suitable platform for testing the material-identification capabilities of our Brewster-enhanced EUV ptychography, particularly its sensitivity to small changes in surface composition introduced by standard nanofabrication and inspection techniques.

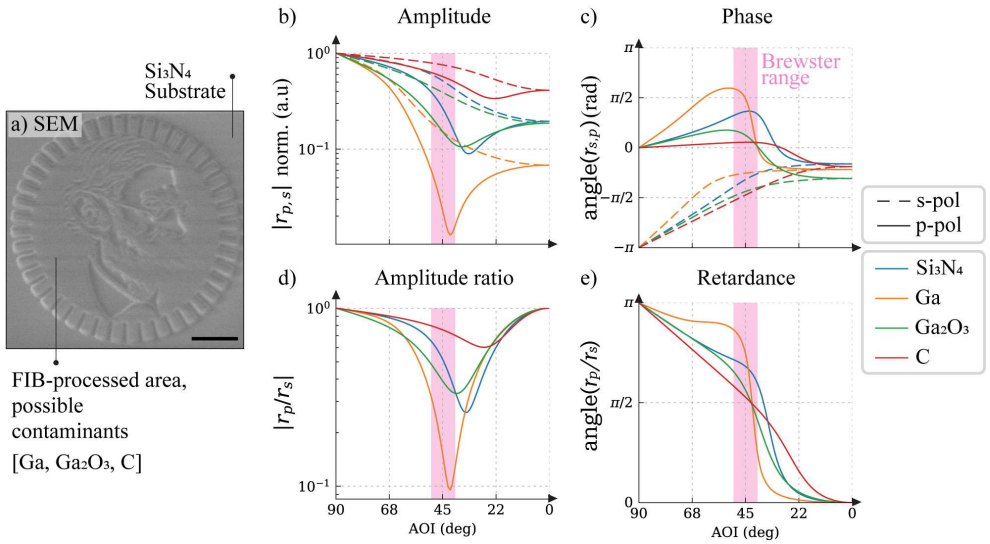


Fig. 3 Abbe portrait test structure and theoretical analysis of contaminants' complex reflectivity. (a) Scanning electron microscopy (SEM) micrograph with labels indicating the substrate and the FIB-processed area. Scale bar: 10 µm. Calculated Fresnel reflection coefficients versus angle of incidence at $E = 26.7$ eV for Si_3N_4, Ga, Ga_2O_3, and C. (b-c) Amplitude and phase of the s- (dashed) and p-polarised (solid) coefficients r_s and r_p. (d-e) Amplitude $|\rho|$ and phase angle(ρ) of the complex ratio $\rho = r_p/r_s$. The shaded band ($45° \pm 5°$) marks the Brewster-like angular range, where diattenuation and retardance are enhanced for each material, and their responses become clearly distinct from one another.

We aim to distinguish the response of the FIB-milled surface from that of the surrounding Si_3N_4 substrate from two polarisation-resolved ptychographic reconstructions. Based on the SEM/FIB processing history, we consider Si_3N_4, Ga, Ga_2O_3 (as an oxidised Ga phase), and C as plausible surface species [45, 46], and use the Fresnel equations to assess how well these materials can be separated at a single angle of incidence. We calculate the complex reflection coefficients $r_p(\theta)$ and $r_s(\theta)$ at 26.7 eV for angles of incidence between 0° and 90°, assuming bulk interfaces (see Supplemental document for optical-constant details). Panels b) and c) in Fig. 3 show the corresponding amplitudes and phases. From these, we compute for each material the *complex reflection ratio* [47]

$$\rho = \frac{r_p}{r_s},$$

and plot its amplitude $|\rho|$ and retardance angle (ρ) in the lower panels d) and e). In the Brewster range, the p-polarised reflection coefficient r_p not only reaches a pronounced minimum in magnitude but also exhibits a rapid variation in phase, whereas r_s changes more slowly with angle. As a result, small differences in the complex refractive index lead to large changes in both the amplitude ratio (characterising the *reflective diattenuation*) and phase (*retardance*) of ρ. This identifies the Brewster-range (e.g. $\theta_i \approx 45°$)

as a robust single-angle operating point for material discrimination in our experiment: it enhances diattenuation and retardance, and the candidate materials occupy well-separated regions in the complex ρ plane.

Experimental validation

We measured the "Abbe portrait" at AOI of 45° under s- and p-polarised illumination in order to access this Brewster-enhanced contrast experimentally. After phase-referencing the two reconstructions (see Methods, Section 4.6), we form the experimental complex reflection ratio $\rho(\mathbf{r}) = r_p(\mathbf{r})/r_s(\mathbf{r})$, and map the response of each pixel to a specific location in the complex plane. Rather than relying solely on manually selected regions of interest, we assess the material discrimination in an unsupervised model-based clustering by analysing the two-dimensional distribution of ρ values. (An ROI-based cluster analysis of selected regions is provided in the Supplemental document for comparison.) The left panel of Fig. 4 shows a log-scaled 2D histogram of ρ in the complex plane, with iso-density contours. Two pronounced peaks are apparent, suggesting two dominant material responses across the sample. We therefore fit a two-component Gaussian mixture model (GMM; see Methods) to the full ρ distribution for cluster identification. Mapping the pixels from those clusters back to spatial coordinates allows for spatially resolved segmentation or unmixing. Thus, for each pixel, we evaluate the assignment probabilities $P(z = k \mid \rho)$, where z denotes cluster membership. The iso-density contours are coloured according to the model's equal-assignment decision boundary ($P = 0.5$), highlighting the separation between the two modes in ρ-space; the GMM means and the theoretical reference values of ρ for the candidate materials are shown for orientation. Next to this histogram (panel b), we plotted the signed contrast

$$C_\rho = P(z = 1 \mid \rho) - P(z = 0 \mid \rho),$$

to visually assess the spatial distribution. In C_ρ, contrast values close to $+1$ or -1 indicate pixels that are strongly assigned to component 1 or component 0, respectively, whereas values near zero correspond to a balanced assignment between the two components. The map reveals two spatially contiguous domains that separate the FIB-milled region from the surrounding membrane, demonstrating a systematic difference in the polarisation-dependent complex response, consistent with a change in surface composition. Between these domains, pixels with scores near zero mark a transition region where the posterior is locally balanced between the two components. The intermediate-score region forms a patchy, splattered pattern around the milled area rather than a smooth boundary. This suggests a heterogeneous near-surface modification, for example, due to local carbonaceous contamination and Ga implantation and redeposition during FIB milling.

In the second row of Fig. 4c-e), we compare our EUV-based probability map (e) with two standard tools for material identification, namely EDX (c) and ToF-SIMS (d). These measurements were performed on a replica "Abbe portrait" sample to ensure comparable conditions. In all three modalities, the presence of Ga as a primary contaminant is clearly confirmed on the FIB-processed area, but the trade-offs are evident. Because of the low sensitivity to thin surface layers, larger interaction volume, and lower fluorescent yield of the electron beam, the EDX map exhibits a coarser

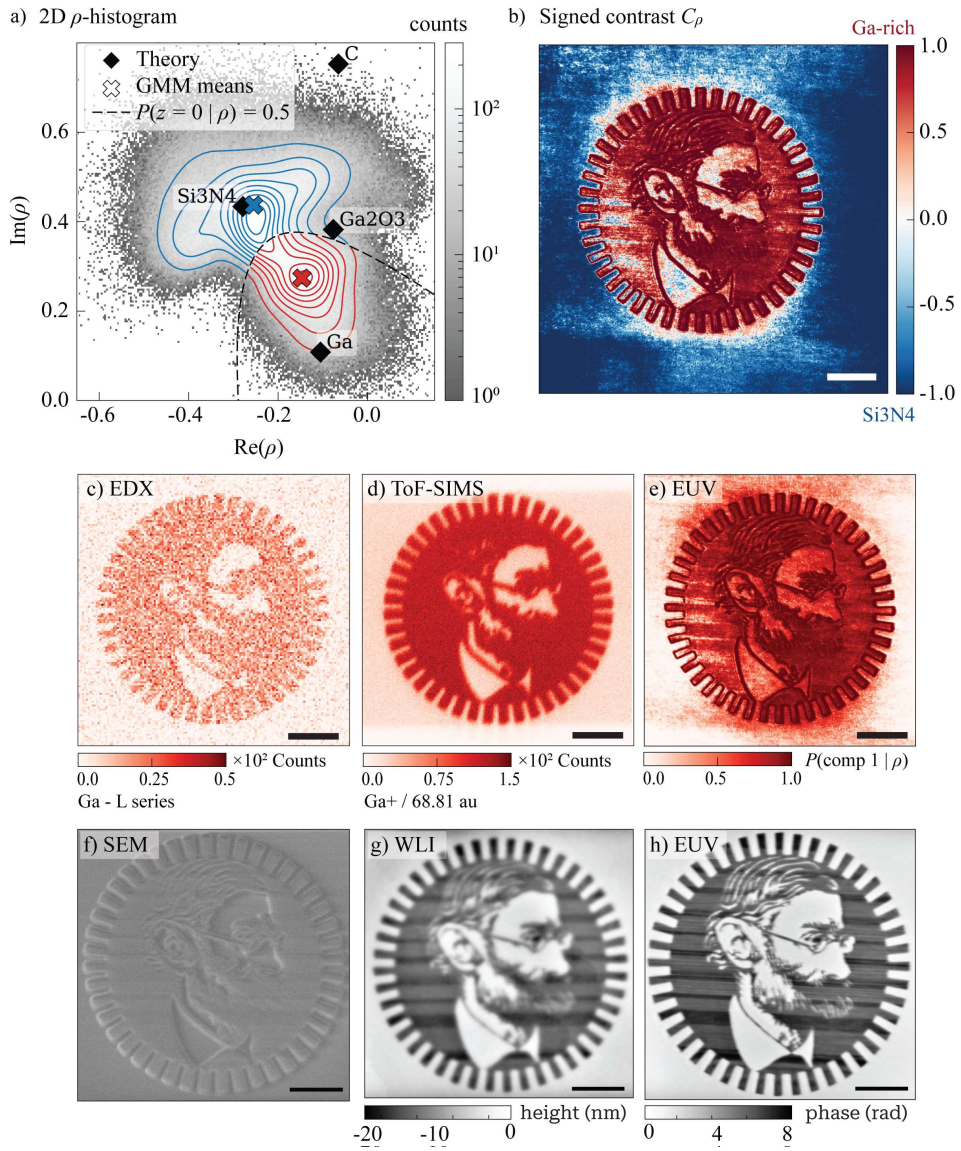


Fig. 4 Summary of metrology results on the Abbe portrait. (a) Log-scaled 2D histogram of measured ρ values with iso-density contours; a two-component GMM is overlaid (component means and the $P(z = k \mid \rho) = 0.5$ decision boundary). Theoretical ρ values for candidate materials are shown as reference markers. (b) Spatial map of the signed assignment contrast C_ρ, separating the FIB-milled region from the surrounding membrane. (c) EDX map of the Ga L-series (around 1.1 keV), acquired at an accelerating voltage of 10 kV. (d) Cumulative ToF-SIMS map of Ga^+ ions after 150 nm sputtering. (e) Assignment probability map $P(\text{comp } 1 \mid \rho)$ from our EUV Brewster-range approach. (f) SEM micrograph. (g) WLI height map (50× objective). (h) Unwrapped phase from EUV reflection ptychography encoding topographic information. Scale bar: 10 µm.

effective spatial resolution and a lower signal-to-noise ratio for this particular sample. By contrast, the ToF-SIMS maps provide higher spatial resolution and higher SNR, but at the cost of ablating the surface and thereby destroying the sample. Our EUV probability map, in turn, is obtained non-destructively and is intrinsically sensitive to nanometre-scale surface contaminants rather than a larger interaction volume, while still providing a spatially resolved material discrimination of the modified surface area. In addition, the lower panels in Fig. 4f-h), compare the unwrapped phase from a single polarisation measurement (h) with a WLI height map (g) and the initial SEM micrograph (f). The unwrapped phase encodes the surface topography: all topographic features are clearly visible as phase variations with higher contrast than in the SEM micrograph, and fine structures that appear blurred in the WLI image are sharply resolved.

2.3 Throughput evaluation

Here we define throughput as the effective number of reconstructed image pixels P_{eff} per total acquisition time T_{acq}:

$$\text{Throughput} = \frac{P_{\text{eff}}}{T_{\text{acq}}} = \frac{A_{\text{rec}}/\delta x^2}{T_{\text{acq}}} \quad [\text{Mpx}\,\text{h}^{-1}],$$

where the effective pixel count is given by the reconstructed sample area A_{rec} divided by the achieved lateral resolution δx squared (as determined from the FRC 1/2-bit criterion [43]), and the acquisition time includes exposure, detector readout, and stage overhead (see Supplement document for details). We deliberately exclude the reconstruction time from this definition, since longer reconstruction times can be improved independently by increasing computational resources, optimising reconstruction pipelines, or both. Our reconstructions for instance, were performed on a workstation with an Intel Xeon processor and a 48GB NVIDIA RTX-A6000, taking around 30 minutes.

Previous reflection ptychography experiments with tabletop sources have typically operated at substantially lower throughput levels. Our highest throughput of $\sim$ 100 $\text{Mpx}\,\text{h}^{-1}$ corresponds to nearly two orders of magnitude increase over earlier demonstrations [20–25] and falls within the range of reported values for synchrotron-based implementations [33–36].

We summarise our single-dataset throughput values in Fig. 5, together with reported values for other EUV reflection ptychography experiments. We emphasise that this should not be regarded as a direct, like-for-like performance comparison, as each method targets different material systems, spectral ranges, and measurement configurations; rather, the figure is intended to provide an order-of-magnitude context for where our tabletop approach sits within the current landscape.

For a single s-polarisation measurement on the Si_3N_4 substrate, the highest-throughput configuration (86 % overlap) reaches $\sim$ 100 $\text{Mpx}\,\text{h}^{-1}$. In a more strongly overlapped scan (94 %), the throughput is $\sim$ 20 $\text{Mpx}\,\text{h}^{-1}$ for a single-exposure s-polarised dataset and $\sim$ 10 $\text{Mpx}\,\text{h}^{-1}$ for a high-dynamic-range s-polarised acquisition.

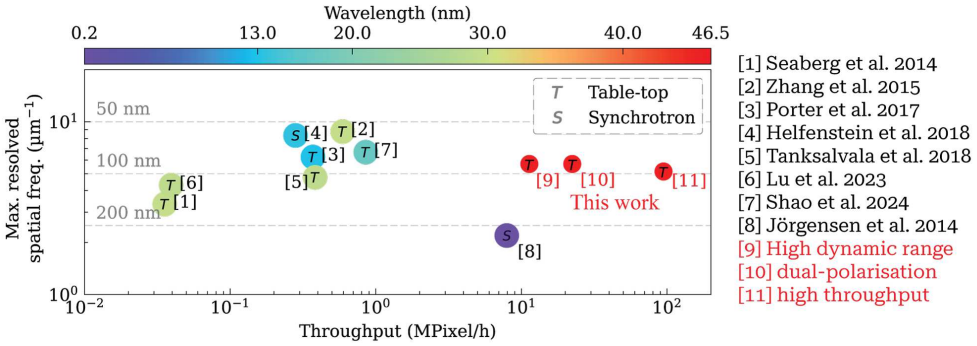


Fig. 5 Comparison of single-dataset throughput for EUV reflection ptychography experiments. Our tabletop configurations are shown together with reported values from previous tabletop and synchrotron-based reflection ptychography. Data taken from [20–25, 33, 34]. Adapted from [48].

The specific configurations and their throughputs are summarised in the Supplemental document.

3 Discussion

Conceptually, our approach bridges the gap between conventional EUV ellipsometry and coherent imaging. Rather than sampling a high-dimensional space of incidence angles and polarisations, we trade measurement diversity for a regime in which the intrinsic material contrast is maximised and the complex-valued response is retrieved via ptychography. This makes EUV material characterisation more compatible with tabletop sources and provides a high-resolution tool that is sensitive to thin, few-nanometre surface components.

We demonstrate that Brewster-range EUV reflection ptychography, driven by a high-flux tabletop HHG source and a deliberately structured illumination probe, can deliver quantitative surface metrology, single-angle two-polarisation material discrimination, and throughput levels that are no longer flux-limited but predominantly bounded by stage overhead time. For a single s-polarisation measurement on the Si_3N_4 substrate, and low overlap configuration, we reach up to $\sim 100\ \mathrm{Mpx\,h^{-1}}$, corresponding to nearly two orders of magnitude increase over previous reflection ptychography with tabletop sources [20–25] and falling within the range of reported throughput levels for synchrotron-based implementations [33–36]. Such performance is enabled by our milliwatt-class HHG source combined with a fast sCMOS detector, and indicates that further gains could be realised by faster scanning hardware, continuous-scan acquisition, or optimised scan trajectories.

The metrology results on a standard USAF test target, demonstrate that the phase-derived height maps agree closely with AFM while bypassing scan-line artefacts and resolution-FOV trade-offs limits. While phase unwrapping is required to resolve larger topographic features, a combination with multispectral ptychography approaches, could further help the identification of multiple phase jumps $> 2\pi$[49–51]. On a FIB-fabricated Abbe portrait, the reconstructions provide both Ångstrom-scale height sensitivity, diffraction-limited lateral resolution, and polarisation-dependent

complex reflectivities $r_{s,p}$ that discriminate different near-surface material states in the complex-ρ plane. By exploiting the enhanced material contrast in ρ near the Brewster range, we achieve quantitative discrimination between Si_3N_4 substrate and the Ga-rich FIB-processed areas on a Si_3N_4-based test structure.

Furthermore, in contrast to the lower SNR and destructive approach of EDX and ToF-SIMS, our material identification maps show higher SNR, higher spatial resolution, and are obtained non-destructively with co-registered height information from the reconstructed phase. This combination facilitates cross-correlation analysis aimed at identifying topographical or contaminant features in material applications, while preserving the sample under investigation.

Looking ahead, the same single-angle, two-polarisation scheme is directly applicable to a broader class of systems where EUV contrast is strong, including two-dimensional materials and their heterostructures, patterned EUV optics and multilayer stacks, and magnetic-domain imaging at resonant absorption edges [52]. With increasing photon flux at higher photon energies, the approach is also promising for at-wavelength characterisation of nanostructures. Coupling the present scheme to pump–probe geometries would additionally enable ultrafast studies in these systems, while preserving quantitative material sensitivity.

Beyond these solid-state applications, the general strategy of combining structured illumination, ptychography and polarisation contrast is, in principle, applicable to recent studies in the EUV [53] to resolve bi-refringence of nanoscale biological structures. More generally, our Brewster-range EUV reflection ptychography provides a practical route to EUV inspection and material-sensitive metrology with high cadence and close co-location with nanofabrication tools, offering a laboratory-based complement to synchrotron EUV material characterisation.

4 Online Methods

In the following, we describe the FIB-milled sample preparation, EUV source and beamline, ptychographic reconstruction, and data-analysis procedures for material identification from polarisation-resolved measurements.

4.1 FIB-milled sample fabrication

The binary "Abbe portrait" test structure was milled into 200 nm-thick Si_3N_4 membranes using a focused Ga^+ ion beam (30 kV, 240 pA beam current, 1260 s total milling duration) in a dual-beam SEM/FIB system (Auriga 40, ZEISS Microscopy). The software module Feature Mill v1.02 (ZEISS SMT) was used for performing the milling process. The test structure was specified as a binary bitmap file, and the scan job was performed using Feature Mills bitmap patterning function.

4.2 EUV source and beamline

The reflection ptychography setup is driven by a milliwatt-class tabletop high-harmonic generation (HHG) source, similar to Ref. [32]. The system operates at a driving wavelength of 515 nm, with 20 fs pulses at a repetition rate of 100 kHz and

a pulse energy of 47 µJ at focus. The laser is actively stabilised during operation and is focused into an argon gas-jet target at 2 bar, generating harmonics around 26.7 eV with a photon flux on the order of 10^{14} ph s^{-1} eV^{-1} at the source. The polarisation of the driving laser, and thus of the generated EUV radiation, is controlled by a half-wave plate (HWP). The resulting higher harmonic spectrum is separated from the fundamental using an annular mirror configuration [54], followed by a 200 nm Al filter for additional suppression of the driving field.

A simplified schematic of the EUV beamline is shown in Fig. 6a), highlighting the main components used for our reflection ptychography experiments. The beamline includes optics for polarisation control and two sets of multilayer mirrors for spectral selection and focusing of the 11th harmonic at 26.7 eV. The EUV photon flux at the source and the reflectivity of the multilayer mirrors are shown in panel b. The EUV beam is focused slightly upstream of an amplitude mask that tailors its wavefront; this mask is positioned approximately 370 µm before the sample. The sample is mounted on an XY-SmarAct stage (XY-CLS32:32) with interferometric position control. The reflected EUV signal is recorded on a 2048 × 2048-pixel Andor sCMOS detector with a pixel size of 11 µm. The lateral extent of the detector and its distance from the sample correspond to a collection numerical aperture NA ~ 0.25.

4.3 Structured illumination

The benefits of structured illumination in ptychography have been demonstrated extensively in transmission geometries [37–41]. In our implementation, we generate a structured EUV probe by modulating the wavefront with an amplitude mask that follows the spiral-mask concept introduced in previous works [39, 41] with the layered structure shown in Fig. 6b) and two main modifications for our reflection geometry: first, we increased the aspect ratio of the nominally circular spiral pattern by a factor of $\sqrt{2}$ along the horizontal direction to match the beam footprint under 45° incidence. In this geometry, the EUV beam illuminates the mask with an elliptical profile that is elongated by a factor $1/\cos 45° = \sqrt{2}$ along the tilt axis, so stretching the spiral in this direction allows the structured aperture to better capture the impinging beam and maximise the transmitted photon flux. Second, we adjusted the spiral fill factor from 50 % to 70 % as a heuristic compromise that increases the transmitted photon flux without sacrificing the wavefront-tailoring capability of the original design. In addition, Fig. 6b) shows an important design element: an Aluminum wall that sits between the mask opening and the large aperture that allows the collection of the main scattering. This wall suppresses any back-scattering light coming from the mask and thus allows a clean measurement of the signal coming from the sample. For comparison, a diffraction pattern recorded with and without this blocking structure is shown in panel d. Additional details can be found in the Supplemental document.

4.4 Data acquisition

Optimal reconstruction of ptychographic datasets depends not only on the employed computational algorithm, but also on acquiring high-quality data. Here we briefly describe our acquisition routine. For a given scan area, we choose the number of scan

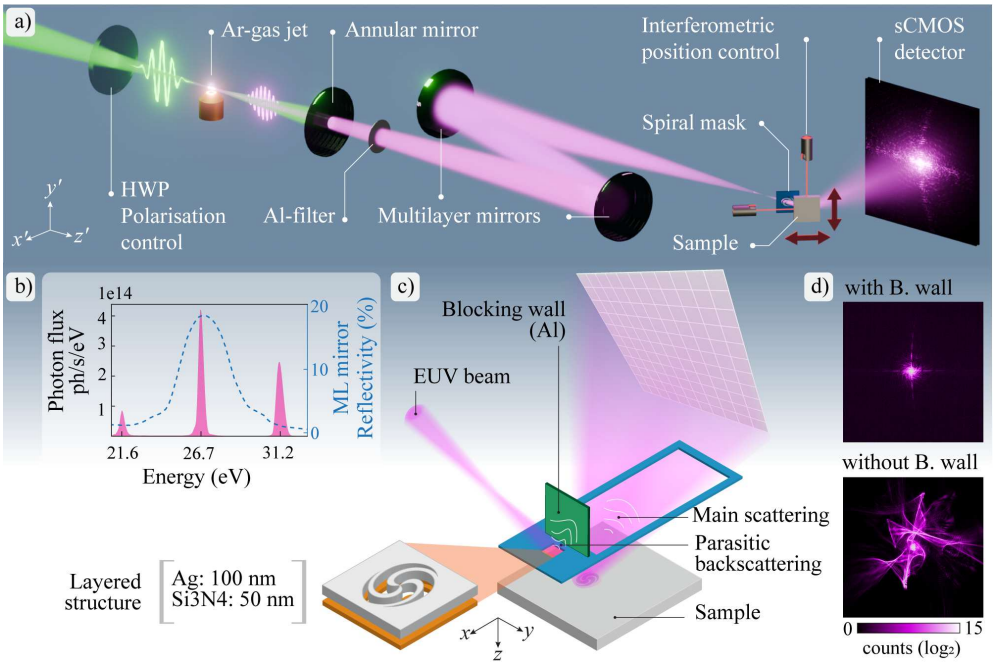


Fig. 6 Schematic of the tabletop EUV beamline and the structured mask used for reflection ptychography. a) The high-harmonic beam is generated in an argon gas-jet target, spectrally filtered and focused by multilayer mirrors, and structured by a mask before reaching the sample. The reflected EUV signal is recorded on an sCMOS detector placed with a collection numerical aperture NA ~ 0.25. b) Measured photon flux at source and reflectivity profile of multilayer mirrors for spectral selection. c) Patterned layered structure of spiral aperture and adjacent, larger collection aperture for the reflected beam. A thin blocking wall (green) is integrated into the mask holder at the boundary between the two apertures to block back-scattered signal from the opaque regions of the mask while preserving the desired collection numerical aperture. d) Comparison of a diffraction pattern with and without a blocking wall.

positions to ensure an overlap of at least 85 % between adjacent probe positions. We use a Fermat-spiral distribution of scan points to maximise the uniformity of the overlap and to reduce reconstruction artefacts [55]. The total travel distance, and thus the scan time, is minimised by solving a travelling-salesman problem for the set of scan positions. The exposure time is chosen such that only a small number of detector pixels reach saturation. For high-dynamic-range (HDR) measurements, we acquire a second dataset with an exposure time at least ten times longer and merge the two exposure levels using a Bayesian approach [56]. During acquisition, we monitor the stage stability to ensure that vibrations remain below or comparable to the projected real-space pixel size (89 nm). After each scan, we close the Ar gas flow to stop the HHG process and record a set of background frames (typically 20). From these frames, we compute a per-pixel map of the background mean and subtract it from each raw diffraction pattern as a first pre-processing step. The specific acquisition parameters for the datasets are summarised in the Supplemental document.

4.5 Ptychographic reconstruction

Each background-corrected diffraction dataset is further pre-processed before ptychographic reconstruction. We interpolate them into a regular frequency space grid to account for the non-coplanar detection geometry [57] (see Supplemental document). We use the open-source code *PtyLab* [58] for ptychographic reconstruction. In particular, we employ the gradient-based iterative mPIE engine [59] with a mixed-state probe model (with four modes) [60] and an additional background estimation [61] to account for partial spatial coherence of the source and residual background noise. Although the EUV radiation is generated from a coherent laser, small fluctuations in the driving laser and mechanical vibrations on the order of a few tens of nanometres from neighbouring equipment can degrade the measured speckle patterns and reduce reconstruction quality. During reconstruction, we do not enforce zero intensity outside the interpolated spatial frequency range in reciprocal space. Only this interpolated region is constrained by the measured data; the remaining Fourier pixels are left unconstrained, in analogy with missing-data formulations used in super-resolution ptychography [62]. To improve the reconstruction quality further, we refine the sample–detector distance estimation by maximising the probe purity metric [63].

4.6 Complex reflection ratio and material identification

For each polarisation state, the reconstruction yields a complex object, $\widetilde{O}_s(\mathbf{r})$ and $\widetilde{O}_p(\mathbf{r})$, that encodes both the surface topography and the local optical response. Assuming that the illumination and detection conditions are unchanged between the s- and p-polarised measurements, and that surface roughness is effectively polarisation independent, we can take the ratio of the reconstructed objects,

$$\frac{\widetilde{O}_p(\mathbf{r})}{\widetilde{O}_s(\mathbf{r})} = \frac{A(\mathbf{r})\exp\big[i\phi_{\mathrm{OPD}}(\mathbf{r})\big]\widetilde{r}_p(\mathbf{r})}{A(\mathbf{r})\exp\big[i\phi_{\mathrm{OPD}}(\mathbf{r})\big]\widetilde{r}_s(\mathbf{r})} = \frac{\widetilde{r}_p(\mathbf{r})}{\widetilde{r}_s(\mathbf{r})} \equiv \rho(\mathbf{r}).$$

Under these assumptions, both the geometrical phase and any polarisation-independent amplitude factor cancel, and the *complex reflection ratio* $\rho(\mathbf{r})$ directly probes the local polarisation-dependent reflectivity. In practice, however, each ptychographic reconstruction is determined only up to an arbitrary complex scalar, so $\widetilde{O}_s$ and $\widetilde{O}_p$ can differ by independent global phase and amplitude offsets. As a result, the raw ratio $\widetilde{O}_p(\mathbf{r})/\widetilde{O}_s(\mathbf{r})$ does not directly yield the physical $\rho(\mathbf{r})$, because the relative phase between the s- and p-polarised responses is not fixed.

To obtain a physically meaningful ratio, we correct these offsets using a reference ROI that we expect to consist of bulk Si_3N_4. This ROI is chosen far from the FIB-milled area and outside the region exposed to SEM imaging, so that damage and contamination are minimised. In this ROI, the reflectivity is well described by the Fresnel coefficients [64]

$$r_s = \frac{n_1\cos\theta_i - n_2\cos\theta_t}{n_1\cos\theta_i + n_2\cos\theta_t}, \qquad r_p = \frac{n_2\cos\theta_i - n_1\cos\theta_t}{n_2\cos\theta_i + n_1\cos\theta_t}, \tag{1}$$

where $n_1 = 1$ (vacuum), $n_2 = 1 - \delta + i\beta$ is the complex refractive index at the photon energy of interest, and θ_t is the complex transmission angle determined by Snell's law.

We compute the theoretical Fresnel coefficients r_s and r_p for Si_3N_4 at 26.7 eV and $\theta_i = 45°$ using an index $n_2 = 1 - 0.303 + i0.137$. The values of δ and β for Si_3N_4 are computed from the tabulated atomic scattering factors f_1 and f_2 in the Chantler dataset (accessed via `xraydb` [65]) using the standard relation [66]

$$\delta + i\beta = (r_e \lambda^2 / 2\pi) \sum_j n_j \, [Z_j + f_{1,j} + i f_{2,j}],$$

with n_j the atomic number densities derived from the stoichiometric composition and mass density of Si_3N_4 [29]. The resulting complex refractive index for Si_3N_4 follows the expected trend of CXRO-based optical constants at higher energies and extrapolates smoothly below 30 eV (see Supplementary information).

We then determine complex scalars c_s and c_p such that

$$c_s \, \langle \widetilde{O}_s \rangle_{\mathrm{ROI}} = r_s, \qquad c_p \, \langle \widetilde{O}_p \rangle_{\mathrm{ROI}} = r_p,$$

where $\langle \widetilde{O}_{s,p} \rangle_{\mathrm{ROI}}$ denotes the mean complex value of the corresponding reconstruction over the reference ROI. The referenced complex reflection ratio is then defined as

$$\rho(\mathbf{r}) = \frac{c_p \, \widetilde{O}_p(\mathbf{r})}{c_s \, \widetilde{O}_s(\mathbf{r})},$$

which yields a physically referenced ratio $\rho(\mathbf{r})$. After this referencing, the distribution of ρ in the complex plane is centred near the theoretical value for Si_3N_4 (see Fig. 4a in the Results section).

To identify regions with distinct optical responses, we assess the 2D-histogram distribution of the complex ratio $\rho(\mathbf{r})$, and we perform Gaussian mixture modeling (GMM) as an unsupervised learning algorithm to cluster the two visible peaks in Fig.4a). The fitted GMM model used standard matrices and an expectation–maximisation algorithm as implemented in `scikit-learn` [67]. Mapping the pixels from the fitted clusters back to spatial coordinates allows for spatially resolved segmentation. This is achieved by evaluating the assignment probabilities $P(z = k \mid \rho(\mathbf{r}))$, where z denotes cluster membership for each component $k \in \{0, 1\}$ at every pixel. We visualise the spatial unmixing as the signed contrast

$$C_\rho(\mathbf{r}) = P(z = 1 \mid \rho(\mathbf{r})) - P(z = 0 \mid \rho(\mathbf{r})),$$

as shown in Fig. 4b) in the Results section. This constitutes an unsupervised segmentation of the field of view based solely on the measured complex reflection ratios.

Acknowledgements. We thank Stephanie Lippmann, Dongmei Liu and Katharina Freiberg for valuable discussions on overlayer contamination and Ga^+ implantation

induced by FIB processing. We thank Stephan Gierth for performing ToF-SIMS analysis.

Funding. Fraunhofer-Gesellschaft (Cluster of Excellence Advanced Photon Sources); Helmholtz Association (Ptychography 4.0, ZT-I-PF-4-018 (AsoftXm)); Supported by the Free State of Thuringia and the European Social Fund Plus (2023FGR0053); Deutsche Forschungsgemeinschaft (DFG, German Research Foundation) – Project number 405054418; BMFTR under project EXSAM (13N16673).

Author contributions. J.R. and J.L. conceived the project. D.P. and M.A. designed the EUV reflection ptychography setup. M.A. implemented and operated the HHG source and beamline. D.P. designed and implemented the data-acquisition system for the ptychography experiments. R.B. fabricated the spiral mask and FIB-milled test structures, and performed SEM, WLI, and EDX measurements. D.P. and M.A. acquired the ptychographic datasets. D.P. performed the ptychographic reconstructions, FRC analysis, and ρ-based material-identification analysis, prepared the figures, and wrote the first draft of the manuscript with input from J.R., R.K., T.S., W.E., M.A., C.L., and L.L. All authors discussed the results and contributed to the final manuscript. J.R. and R.K. supervised the project.

Competing interests. The authors declare no competing interests.

Data Availability. The data that support the findings of this study are available from the corresponding author, upon reasonable request.

Code availability. Ptychographic reconstructions were performed using the open-source PtyLab package [58], which is available at Github.com/PtyLab/PtyLab.py.

Supplementary information. See Supplementary Information for supporting content

References

[1] Kazazis, D., Santaclara, J. G., van Schoot, J. *et al.* Extreme ultraviolet lithography. *Nature Reviews Methods Primers* **4**, 84 (2024). URL https://doi.org/10.1038/s43586-024-00361-z.

[2] Castellanos-Gomez, A., Duan, X., Fei, Z. *et al.* Van der waals heterostructures. *Nature Reviews Methods Primers* **2**, 58 (2022). URL https://doi.org/10.1038/s43586-022-00139-1.

[3] Hwang, H. Y. *et al.* Emergent phenomena at oxide interfaces. *Nature materials* **11**, 103–113 (2012).

[4] Zhou, K. *et al.* Emerging 2d metal oxides: from synthesis to device integration. *Advanced Materials* **35**, 2207774 (2023).

[5] Evans, D. M., Garcia, V., Meier, D. & Bibes, M. Domains and domain walls in multiferroics. *Physical Sciences Reviews* **5**, 20190067 (2020).

[6] Chen, H.-T., Taylor, A. J. & Yu, N. A review of metasurfaces: physics and applications. *Reports on progress in physics* **79**, 076401 (2016).

[7] Solntsev, A. S., Agarwal, G. S. & Kivshar, Y. S. Metasurfaces for quantum photonics. *Nature Photonics* **15**, 327–336 (2021).

[8] Liu, W. *et al.* Probing the buried magnetic interfaces. *ACS applied materials & interfaces* **8**, 5752–5757 (2016).

[9] Choi, J. I. J., Kim, T.-S., Kim, D., Lee, S. W. & Park, J. Y. Operando surface characterization on catalytic and energy materials from single crystals to nanoparticles. *ACS nano* **14**, 16392–16413 (2020).

[10] Mochi, I. *et al.* Gargini, P. A., Naulleau, P. P., Ronse, K. G. & Itani, T. (eds) *Actinic inspection of euv reticles with arbitrary pattern design.* (eds Gargini, P. A., Naulleau, P. P., Ronse, K. G. & Itani, T.) *International Conference on Extreme Ultraviolet Lithography 2017*, Vol. 10450, 28–37. SPIE (SPIE, 2017).

[11] Kazazis, D., Santaclara, J. G., van Schoot, J., Mochi, I. & Ekinci, Y. Extreme ultraviolet lithography. *Nature Reviews Methods Primers* **4**, 84 (2024).

[12] Yang, S. & Zhang, G. A review of interferometry for geometric measurement. *Measurement Science and Technology* **29**, 102001 (2018).

[13] Harasaki, A., Schmit, J. & Wyant, J. C. Offset of coherent envelope position due to phase change on reflection. *Applied Optics* **40**, 2102–2106 (2001).

[14] Trache, A. & Meininger, G. A. Atomic force microscopy (afm). *Current protocols in microbiology* **8**, 2C–2 (2008).

[15] Newbury*, D. E. & Ritchie, N. W. Is scanning electron microscopy/energy dispersive x-ray spectrometry (sem/eds) quantitative? *Scanning* **35**, 141–168 (2013).

[16] Brundle, C., Conti, G. & Mack, P. Xps and angle resolved xps, in the semiconductor industry: Characterization and metrology control of ultra-thin films. *Journal of Electron Spectroscopy and Related Phenomena* **178**, 433–448 (2010).

[17] Jia, F., Zhao, X. & Zhao, Y. Advancements in tof-sims imaging for life sciences. *Frontiers in Chemistry* **11**, 1237408 (2023).

[18] Rodenburg, J. & Maiden, A. Ptychography. *Springer Handbook of Microscopy* 819–904 (2019).

[19] Loetgering, L., Witte, S. & Rothhardt, J. Advances in laboratory-scale ptychography using high harmonic sources. *Optics Express* **30**, 4133–4164 (2022).

[20] Seaberg, M. D. *et al.* Tabletop nanometer extreme ultraviolet imaging in an extended reflection mode using coherent fresnel ptychography. *Optica* **1**, 39–44 (2014).

[21] Zhang, B. *et al.* High contrast 3d imaging of surfaces near the wavelength limit using tabletop euv ptychography. *Ultramicroscopy* **158**, 98–104 (2015).

[22] Porter, C. L. *et al.* General-purpose, wide field-of-view reflection imaging with a tabletop 13 nm light source. *Optica* **4**, 1552–1557 (2017).

[23] Tanksalvala, M. *et al.* Nondestructive, high-resolution, chemically specific 3d nanostructure characterization using phase-sensitive euv imaging reflectometry. *Science Advances* **7**, eabd9667 (2021).

[24] Lu, H. *et al.* Characterisation of engineered defects in extreme ultraviolet mirror substrates using lab-scale extreme ultraviolet reflection ptychography. *Ultramicroscopy* **249**, 113720 (2023).

[25] Shao, Y. *et al.* Wavelength-multiplexed multi-mode euv reflection ptychography based on automatic differentiation. *Light: Science & Applications* **13**, 196 (2024).

[26] Shanblatt, E. R. *et al.* Quantitative chemically specific coherent diffractive imaging of reactions at buried interfaces with few nanometer precision. *Nano letters* **16**, 5444–5450 (2016).

[27] Karl Jr, R. M. *et al.* Full-field imaging of thermal and acoustic dynamics in an individual nanostructure using tabletop high harmonic beams. *Science advances* **4**, eaau4295 (2018).

[28] Gouder, M., Zhang, F., Du, M. & Witte, S. *Ptychographic imaging ellipsometry with visible and extreme ultraviolet light*. Optica Publishing Group (Optica Publishing Group, 2025). Paper ch-5-3.

[29] Henke, B. L., Gullikson, E. M. & Davis, J. C. X-ray interactions: photoabsorption, scattering, transmission, and reflection at e= 50-30,000 ev, z= 1-92. *Atomic data and nuclear data tables* **54**, 181–342 (1993).

[30] Calegari, F., Sansone, G., Stagira, S., Vozzi, C. & Nisoli, M. Advances in attosecond science. *Journal of Physics B: Atomic, Molecular and Optical Physics* **49**, 062001 (2016).

[31] Ciriolo, A. *et al.* Microfluidic devices for quasi-phase-matching in high-order harmonic generation. *APL Photonics* **7** (2022).

[32] Klas, R. *et al.* Table-top milliwatt-class extreme ultraviolet high harmonic light source. *Optica* **3**, 1167–1170 (2016).

[33] Helfenstein, P. *et al.* Beam drift and partial probe coherence effects in euv reflective-mode coherent diffractive imaging. *Optics Express* **26**, 12242–12256 (2018).

[34] Jørgensen, P. *et al.* Hard x-ray grazing-incidence ptychography: large field-of-view nanostructure imaging with ultra-high surface sensitivity. *Optica* **11**, 197–204 (2024).

[35] Guizar-Sicairos, M. *et al.* High-throughput ptychography using eiger: scanning x-ray nano-imaging of extended regions. *Optics express* **22**, 14859–14870 (2014).

[36] Jiang, Y. *et al.* Achieving high spatial resolution in a large field-of-view using lensless x-ray imaging. *Applied Physics Letters* **119** (2021).

[37] Guizar-Sicairos, M. *et al.* Role of the illumination spatial-frequency spectrum for ptychography. *Physical Review B – Condensed Matter and Materials Physics* **86**, 100103 (2012).

[38] Odstrčil, M., Lebugle, M., Guizar-Sicairos, M., David, C. & Holler, M. Towards optimized illumination for high-resolution ptychography. *Optics express* **27**, 14981–14997 (2019).

[39] Eschen, W. *et al.* Material-specific high-resolution table-top extreme ultraviolet microscopy. *Light: Science & Applications* **11**, 117 (2022).

[40] Pelekanidis, A. *et al.* Illumination diversity in multiwavelength extreme ultraviolet ptychography. *Photonics Research* **12**, 2757–2771 (2024).

[41] Eschen, W. *et al.* Structured illumination ptychography and at-wavelength characterization with an euv diffuser at 13.5 nm wavelength. *Optics Express* **32**, 3480–3491 (2024).

[42] Gołek, F., Mazur, P., Ryszka, Z. & Zuber, S. Afm image artifacts. *Applied surface science* **304**, 11–19 (2014).

[43] Van Heel, M. & Schatz, M. Fourier shell correlation threshold criteria. *Journal of structural biology* **151**, 250–262 (2005).

[44] Gil, D. L. & Windover, D. Limitations of x-ray reflectometry in the presence of surface contamination. *Journal of Physics D: Applied Physics* **45**, 235301 (2012).

[45] Postek, M. T. An approach to the reduction of hydrocarbon contamination in the scanning electron microscope. *Scanning: The Journal of Scanning Microscopies* **18**, 269–274 (1996).

[46] Huang, J., Löffler, M., Moeller, W. & Zschech, E. Ga contamination in silicon by focused ion beam milling: Dynamic model simulation and atom probe tomography experiment. *Microelectronics Reliability* **64**, 390–392 (2016).

[47] Azzam, R. M., Bashara, N. M. & Ballard, S. S. Ellipsometry and polarized light (1978).

[48] Eschen, W. *et al.* Coherent nanoscale imaging and chemical mapping with compact extreme ultraviolet and soft x-ray sources: Review and perspective. *APL Photonics* **10** (2025).

[49] Batey, D. J., Claus, D. & Rodenburg, J. M. Information multiplexing in ptychography. *Ultramicroscopy* **138**, 13–21 (2014).

[50] Loetgering, L. *et al.* Tailoring spatial entropy in extreme ultraviolet focused beams for multispectral ptychography. *Optica* **8**, 130–138 (2021).

[51] Du, M., Loetgering, L., Eikema, K. S. & Witte, S. Ptychographic optical coherence tomography. *Optics letters* **46**, 1337–1340 (2021).

[52] Richter, J. *et al.* Spectroscopic probe of ultrafast magnetization dynamics in the extreme ultraviolet spectral range. *Physical Review B* **111**, 214423 (2025).

[53] Liu, C. *et al.* Visualizing the ultra-structure of microorganisms using table-top extreme ultraviolet imaging. *PhotoniX* **4**, 6 (2023).

[54] Klas, R., Kirsche, A., Tschernajew, M., Rothhardt, J. & Limpert, J. Annular beam driven high harmonic generation for high flux coherent xuv and soft x-ray radiation. *Optics express* **26**, 19318–19327 (2018).

[55] Huang, X. *et al.* Optimization of overlap uniformness for ptychography. *Optics Express* **22**, 12634–12644 (2014).

[56] Kodgirwar, S. *et al.* Bayesian multi-exposure image fusion for robust high dynamic range ptychography. *Optics Express* **32**, 28090–28099 (2024).

[57] Gardner, D. F. *et al.* High numerical aperture reflection mode coherent diffraction microscopy using off-axis apertured illumination. *Optics express* **20**, 19050–19059 (2012).

[58] Loetgering, L. *et al.* Ptylab. m/py/jl: a cross-platform, open-source inverse modeling toolbox for conventional and fourier ptychography. *Optics Express* **31**, 13763–13797 (2023).

[59] Maiden, A., Johnson, D. & Li, P. Further improvements to the ptychographical iterative engine. *Optica* **4**, 736–745 (2017).

[60] Thibault, P. & Menzel, A. Reconstructing state mixtures from diffraction measurements. *Nature* **494**, 68–71 (2013).

[61] Li, P. *Investigations and improvements in ptychographic imaging.* Ph.D. thesis, University of Sheffield (2016).

[62] Maiden, A. M., Humphry, M. J., Zhang, F. & Rodenburg, J. M. Superresolution imaging via ptychography. *Journal of the Optical Society of America A* **28**, 604–612 (2011).

[63] Liu, C. *et al.* Purity-based self-calibration in ptychography. *Optics Letters* **50**, 1581–1584 (2025).

[64] Saleh, B. E. & Teich, M. C. *Fundamentals of photonics, 2 volume set* (john Wiley & sons, 2019).

[65] Newville, M. *et al.* Xraydb: X-ray reference data in sqlite. https://github.com/xraypy/XrayDB (2023). Python interface accessed via the `xraydb` package.

[66] Jacobsen, C. *X-ray Microscopy* (Cambridge University Press, 2019).

[67] Pedregosa, F. *et al.* Scikit-learn: Machine learning in python. *the Journal of machine Learning research* **12**, 2825–2830 (2011).

Supplementary Files

This is a list of supplementary files associated with this preprint. Click to download.

- EUVSupplement.pdf